GSA Data Repository 2018060

Meilijson et al., 2018, Deep-basin evidence resolves a 50-year-old debate and demonstrates synchronous onset of Messinian evaporite deposition in a non-desiccated Mediterranean: Geology, https://doi.org/10.1130/G39868.1.

1. Seismic interpretation

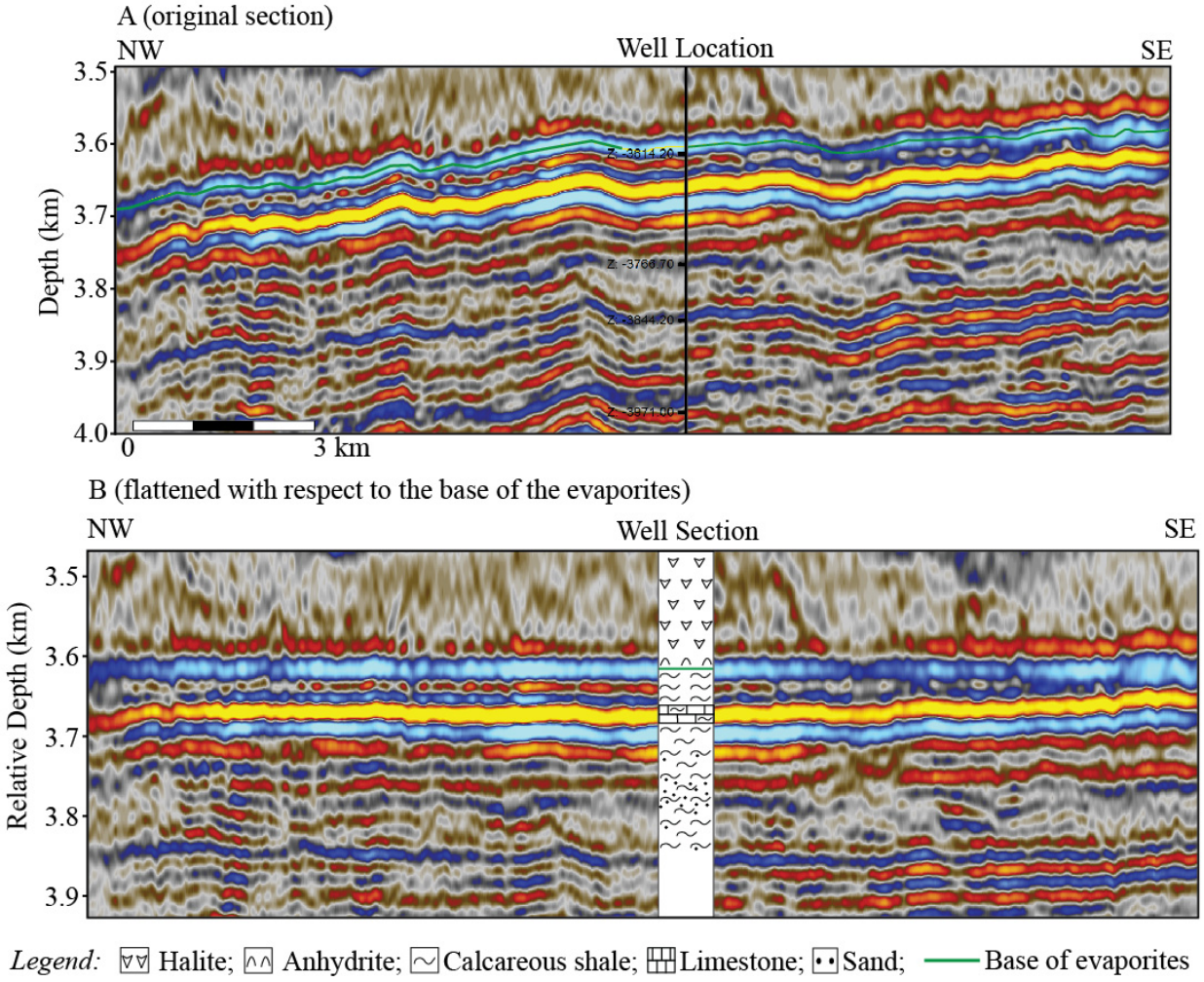

Figure DR1. A sample seismic depth migrated section of the localized 3D commercial dataset, crossing the sampled well location. (A) The original seismic section with a vertical exaggeration of X25. The location of the sampled well is marked by a black line (well location), along which the well tops depths are marked. The interpreted base of evaporites is marked by a green line. (B) The same seismic section flattened with respect to the interpreted base of evaporites. The depth

axis is relative and shifted by 3616 m, to match the depths at the well. A generalized lithological column is incorporated at the well location, corresponding to the legend appearing below.

2. Spectral analysis of well-log curves

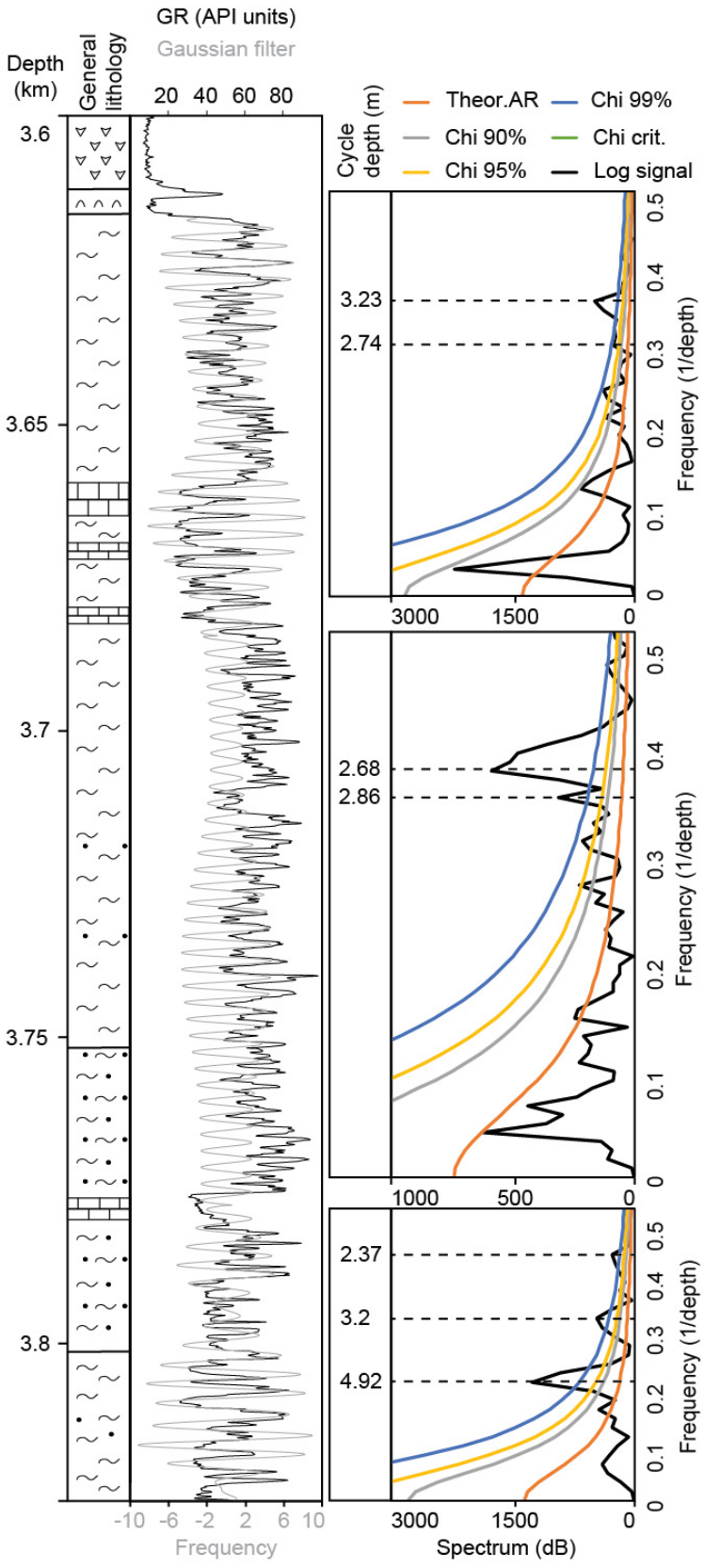

Figure DR2. REDFIT spectral analysis procedure (Schulz and Mudelsee, 2002) was done using PAST and Analyseries software and employed on the gamma ray well log curve. The REDFIT procedure fits the time series to a red noise model null hypothesis (Theor. AR), produces 'false-alarm' parametric approximations (chi2 of 90%, 95%, and 99%) and a 'critical false-alarm' level (chi crit.). The results are presented in the depth-domain. In other words, this procedure identifies statistically validated reoccurring cycles within the data (gray line overlying the GR well log data in Fig. 3, blue line in Fig. DR2), in this case the gamma-ray logs. This process is similar to more traditional cyclostratigeaphic methods in which reoccurring lithological variations are identified and counted, e.g., carbonate/shale transitions. As the data for this study originated from well cuttings it is not possible to identify lithological transitions in high resolution. However, as the GR well log is lithology bound, identified cycles within the GR signal is used here for cyclostratigraphic purposes. REDFIT analyses were run by intervals, defined according to the logs expression and determined by homogeneous standard deviations of the well log data, resulting in these three intervals: (1) 3825-3777 m, (2) 3776.9-3684.5, and from (3) 3684.4 m to the base of the first evaporitic bed. Wavelet spectral analysis show frequencies ranging from 2.37 to 4.92 m, averaging on 3.1 m for the three different intervals. Each interval was filtered (Gaussian bandpass filtering) using the higher confidence frequencies as determined by the REDFIT analysis: (1) 0.3±0.1; (2) 0.37±0.014; (3) 0.365 ± 0.034. See figure DR1 for lithological legend.

3. X-ray diffraction (XRD) and scanning electron microscope (SEM) analysis

The studied well was drilled by Noble Energy and partners in 2010, targeting gas reservoirs in the deep Levant Basin (Fig. 1). Cuttings grains were made available for this study and were picked and sorted under a reflected light standard microscope into their lithological counterparts before geochemical and mineralogical analysis. Identification of specific minerals and semi-quantitative minerology of the evaporites, through the recognition of characteristic peak positions based on standard XRD responses, was accomplished using a Rigaku 600 MiniFlex X-Ray Diffractometer (XRD) with a CuKα source. Optically separated uniform phases were powdered and oven-dried before analysis. Samples were loaded by hand and pressed into sample holders. Diffraction analysis was conducted from 3° to 60° 2θ using a step size of 0.03° and integration time of 1 second per step, at 30 kV/10 mA. PDXL and Matlab software were used for identification and semi-quantitative calculation of individual minerals. The average error for most minerals using this method is ±5%.

The evaporite samples are composed of ~90% halite (Fig. DR3), while the other few minerals identified are anhydrite, magnesite and barite, all of which appear at a relative abundance below the detection limit using semi-quantitative analysis.

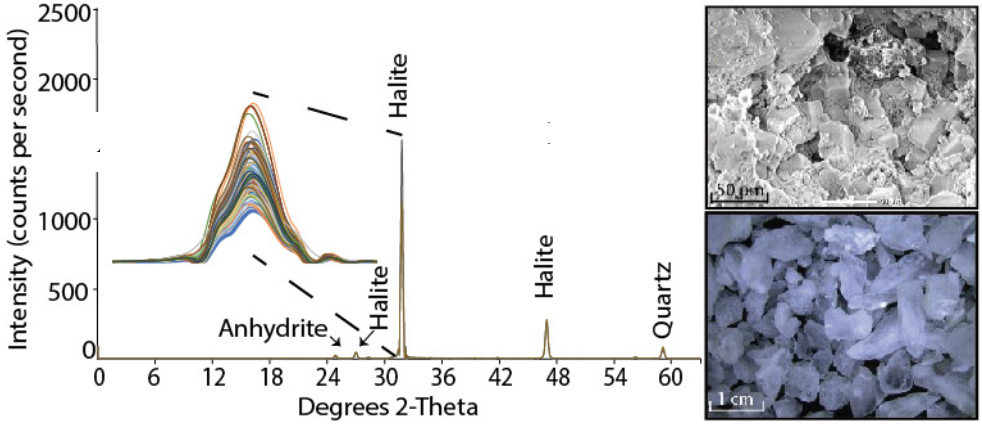

Figure DR3. XRD (left), transmitted light microscopy (center), and SEM (right). Overlaid (color coded) XRD analysis of 89 halite samples produced diffractograms which are practically identical. The main halite peak is zoomed for emphasis. The homogeneous evaporite unit is made of pure halite as seen in hand specimen (center) and SEM imagery of cubic cleavage (right).

4. Biostratigraphy

The biostratigraphic analysis, results, and interpretations are presented in the main text. Here, we recount this analysis and provide further description of the marker species and their interpretation. The only fossil-bearing interval appropriate for biostratigraphy is that of the pre-evaporites, topped by the base of the evaporites. Micropaleontological analysis of foraminifera was employed on a total of 35 samples (well cuttings) containing enough material for reliable biostratigraphy from a depth of 3940 to the base of the evaporites at 3616 m (Table DR1). Each sample represents an interval of 3 m, and there are 6 m between samples. Each bioevent was assigned the average depth of the sample in which it was recognized, although further calculations of sedimentation rates were assigned the whole range (Fig.2). Of the 35 samples, 4 samples contained a high amount of sand and are not suitable for biostratigraphy: 3839.5, 3815.5, 3803.5, and 3776.5 m. Samples for foraminiferal analysis were disaggregated and soaked in a 3% sodium hypochlorite solution for removal of organic matter from the sediment. For biostratigraphic analysis 20 g of each sample were washed and sieved and the larger than 150 μm fraction was analyzed for the identification of different marker species. Planktonic foraminifera were counted in 15 squares of a relatively densely packed standard picking tray. When deemed necessary, additional squares were checked to reliably determine test coiling directions.

The Mediterranean planktonic foraminiferal biostratigraphic zonation of the late Tortonian to Messinian applied in this study is based on zonal schemes and secondary bio-events proposed and astronomically dated by several authors in recent years (Hilgen and Krijgsman, 1999; Husing et al., 2009; Krijgsman et al., 1999; Sierro et al., 2001). The sampling resolution in this study is far less than in the studies of these classical land-based marine sections. However, sampling of the land-based or marginal sections in sub-Milankovich resolution was necessary to build the astrobiochronologic framework of the MSC that is applied here. Moreover, our sampling resolution in the depth domain (i.e., 9 m versus < 20 cm in marginal sections) is partly compensated by the difference in the resolution in the time domain. In this case the sedimentation rate in the pre-evaporites of the studied section (average of 11.5 cm/kyr; Fig. 2) is several times higher than in land-based section such as the Metochia and Pissouri sections (Krijgsman et al., 1995, 2003). Fortunately, the 35 samples made available for the 320 m underlying the base of the evaporites were enough to confidently identify the main bio-events used to construct our age model. Note that we took into consideration the full uncertainties that

stem from the depth uncertainty of the samples and from the age uncertainty of the bio-events to calculate the age for the top of the pre-evaporites (see Fig. 2). Sierro et al. (2001) still incorporated a 3-kyr lagged age for sapropels for astronomical dating of the Abad marls in the Sorbas Basin of Spain (based on age difference between Holocene sapropel S1 and the correlative precession minimum / insolation maximum), while Hüsing et al. (2009) assumed an in-phase relationship without the lag used by Sierro et al. (2001) when dating the sapropel-bearing succession in central Italy. Such a direct response of the North African monsoon (held responsible for sapropel formation) to insolation forcing is suggested by the outcome of climate modeling of orbital forcing (Weber and Tuenter, 2011). The latter approach (no lag) is now generally accepted for older sapropels also because the 3-kyr lag for the youngest Holocene sapropel likely results from the delay of monsoonal intensification as a consequence of the last deglaciation. Consequently, we have corrected the ages of Sierro et al. (2001) by making them 3-kyr older. It should further be realized that Sierro et al. (2001) used the La93 solution for tuning, while Hüsing et al. (2009) used the newer La2004 solution. Ages have been not recalculated but are minimal in the order of 1-kyr on average. Details on the zonal scheme and corresponding datum levels are as follows.

The Last Regular Occurrence (LRO) of *Globorotalia menardii*-4 with an astronomical calibrated age range of 7.718-7.726 Ma and a mean age of 7.722 Ma (Hilgen et al., 1995; Hüsing et al., 2009) is recorded at 3827 m (Table DR1; Fig. 2E). This event is based on the presence of sinistrally coiled *menardii* types of keeled *globorotalids* and is consistent with the *Sphaeroidinellopsis seminulina* and *Globoquadrina altispira* specimens observed in some of the samples below the event.

The next younger event is the First Regular Occurrence (FRO) of the *Globorotalia miotumida* gr., at 3745 m with an age range of 7.240-7.246 Ma and a mean age of 7.23 Ma. The first occurrence of the group in the Mediterranean was often labelled *G. conomiozea* in papers from the eighties and nineties, but equating these two taxa taxonomically led to a relabeling of the event as the first occurrence of the *G. miotumida* group (e.g., Hilgen et al., 1995; Hüsing et al., 2009; Ochoa et al., 2015; Sierro et al., 2001) as that species has priority (i.e., it was defined first). While the studied section is not suited for magnetostratigraphy due to the nature of the samples (low resolution well cuttings), the normal subchron 3Br.1n is located slightly below the FRO of the *G. miotumida* gr., which closely corresponds to the position of the Messinian GSSP (Hilgen

et al., 2000; Hüsing et al., 2009). Consequently, we marked the Tortonian-Messinian boundary with an age of 7.243 Ma at 3745 m. No samples with dominant dextral *G. menardii*-5 were found directly below this event. This can be explained by the relatively coarse sample resolution, although a short hiatus cannot be excluded with certainty.

The next younger event is the top acme of the *Globorotalia scitula* group (dextral forms of the *Globorotalia nicolae* type) with an age range of 6.716-6.717 and a mean age of 6.716 Ma (Sierro et al., 2001) at 3691 m, accompanied by the last occurrence of *G. miotumida*. The interval of dextral coiling of *G. scitula* is rather long at our site, but the main event, the LCO of dextral G. scitula gr., can easily be detected. Also the detection of (rare) dextrally coiled scitula below the main dextral interval (i.e., that of *G. nicolae*) is not uncommon (i.e., Monte del Casino section in Italy (Krijgsman et al., 1997)).

These are followed by the main sinistral to dextral coiling change in the neogloboquadrinids with an age range of 6.348-6.377 and a mean age of 6.363 Ma (Sierro et al., 2001) at 3668.5 m. The 7:9 sinistral-dextral coiling in sample 6 (3668 m; Table DR1) makes it hard to determine whether the association of neogloboquadrinids is dominantly left or right coiling. As the dominance in samples below and above the coiling change is usually > 80-90%, we placed the sinistral to dextral coiling change coincident with sample 6, specifically because similar assemblages with ratio's close to 50% have been found in the interval of the coiling change itself (Sierro et al., 2001).

The youngest event recorded below the transition to the salt unit is the first influx of sinistral neogloboquadrinids above the main coiling change at 3641.5 m, dated in the ramge of 6.110-6.144 and a mean value of 6.127 Ma. The dominance of dextral coiled neogloboquadrinids in the uppermost 2 samples before the base of the evaporites (samples 1 and 2 3616-3634 m; Table DR1) supports the age determined for bioevent 5 (6.127 Ma; e.g., Hilgen and Krijgsman, 1999; Krijgsman et al., 2001; Sierro et al., 2001) suggesting that this is indeed the first influx of sinistral coiled neogloboquadrinids also because the percentage of sinistral specimens is >50%. This influx has been recognized in all the astronomically tuned land-based marine sections (see references above).

The following table summarizes the different ages calculated for the top of the pre-evaporites in the Levant Basin according to the different age ranges and depth uncertainty, leading to differences in average sedimentation rates. The age range provided in the main text includes all

of the following ages. The table presents the two age ranges, the possible sediment thickness between them due to the depth uncertainty of the cutting samples in meters, the time spanning between the two ages in kyr, the outcome of the two possible sedimentation rates, and the resulting min/max/mean ages for the top of the pre-evaporites taking into account the depth uncertainty.

Age range (Ma)	Thickness (m)	Time span (kyr)	Sedimentation rates (cm/kyr)	Pre-ev age min (24 m)	Pre-ev age max (27 m)	Pre-ev age mean (25.5 m)
6.11-6.377	30	267	11.23	5.9	5.88	5.88
	24	267	8.99	5.84	5.81	5.83
6.144-6.348	30	204	14.7	5.98	5.96	5.97
	24	204	11.76	5.94	5.91	5.92

5. Total organic carbon (TOC)

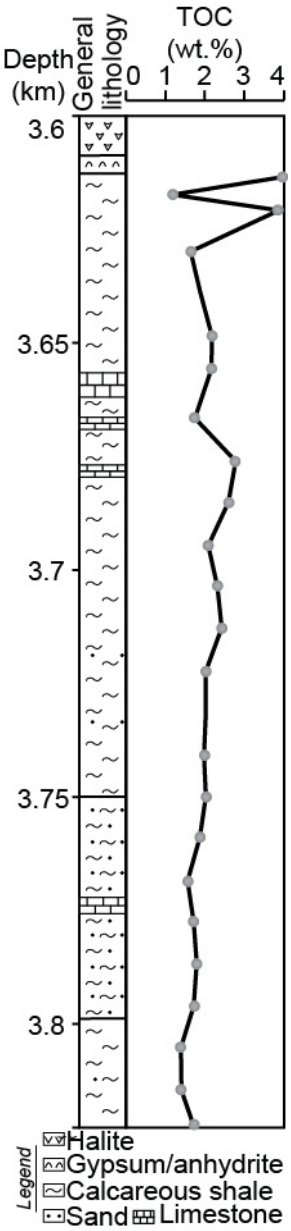

Fig. DR5. TOC was measured using Rock-Eval 6 pyrolysis at Vinci Technologies (France) on a total of 24 shale samples from the studied pre-evaporite section of the Levant Basin. See figure DR1 for lithological legend.

References

Hilgen, F.J., Bissoli, L., Iaccarino, S., Krijgsman, W., Meijer, R., Negri, A., Villa, G., 2000. Integrated stratigraphy and astrochronology of the Messinian GSSP at Oued Akrech (Atlantic Morocco). Earth Planet. Sci. Lett. 182, 237–251. doi:10.1016/S0012-821X(00)00247-8

Hilgen, F.J., Krijgsman, W., 1999. Cyclostratigraphy and astrochronology of the Tripoli diatomite formation (pre-evaporite Messinian, Sicily, Italy). Terra Nov. 11, 16–22. doi:10.1046/j.1365-3121.1999.00221.x

Hilgen, F.J., Krijgsman, W., Langereis, C.G., Lourens, L.J., Santarelli, A., Zachariasse, W.J., 1995. Extending the astronomical (polarity) time scale into the Miocene. Earth Planet. Sci. Lett. 136, 495–510. doi:10.1016/0012-821X(95)00207-S

Hüsing, S.K., Kuiper, K.F., Link, W., Hilgen, F.J., Krijgsman, W., 2009. The upper Tortonian-lower Messinian at Monte dei Corvi (Northern Apennines, Italy): Completing a Mediterranean reference section for the Tortonian Stage. Earth Planet. Sci. Lett. 282, 140–157. doi:10.1016/j.epsl.2009.03.010

Krijgsman, W., Fortuin, A.R., Hilgen, F.J., Sierro, F.J., 2001. Astrochronology for the Messinian Sorbas basin (SE Spain) and orbital (precessional) forcing for evaporite cyclicity. Sediment. Geol. 140, 43–60. doi:10.1016/S0037-0738(00)00171-8

Krijgsman, W., Hilgen, F.J., Negri, A., Wijbrans, J.R., Zachariasse, W.J., 1997. The Monte del Casino section (Northern Apennines, Italy): A potential Tortonian/Messinian boundary stratotype? Palaeogeogr. Palaeoclimatol. Palaeoecol. 133, 27–47. doi:10.1016/S0031-0182(97)00039-4

Krijgsman, W., Hilgen, F.J., Raffi, I., Sierro, F.J., Wilson, D.S., 1999. Chronology, causes and progression of the Messinian salinity crisis. Nature 400, 652–655. doi:10.1038/23231

Laskar, J., Robutel, P., Joutel, F., Gastineau, M., Correia, a. C.M., Levrard, B., 2004. A long-term numerical solution for the insolation quantities of the Earth. Astron. As-trophys. Astron. Astrophys. 428, 261–285. doi:10.1051/0004-6361:20041335

Ochoa, D., Sierro, F.J., Lofi, J., Maillard, A., Flores, J.A., Suarez, M., 2015. Synchronous onset of the Messinian evaporite precipitation: First Mediterranean offshore evidence. Earth Planet. Sci. Lett. 427, 112–124. doi:10.1016/j.epsl.2015.06.059

Schulz, M., Mudelsee, M., 2002. REDFIT: Estimating red-noise spectra directly from unevenly

spaced paleoclimatic time series. Comput. Geosci. 28, 421–426. doi:10.1016/S0098-3004(01)00044-9

Sierro, F.J., Hilgen, F.J., Krijgsman, W., Flores, J.A., 2001. The Abad composite (SE Spain): A Messinian reference section for the Mediterranean and the APTS. Palaeogeogr. Palaeoclimatol. Palaeoecol. 168, 141–169. doi:10.1016/S0031-0182(00)00253-4

Weber, S.L., Tuenter, E., 2011. The impact of varying ice sheets and greenhouse gases on the intensity and timing of boreal summer monsoons. Quat. Sci. Rev. 30, 469–479. doi:10.1016/j.quascirev.2010.12.009

Table DR1. Summary of biostratigraphy

Sample #	Depth from (m)	Depth to (m)	Mean sample depth (m)	*G. miotumida*	*G. menardii-5*	*G. menardii-4*	*G. scitula*	neogloboquadrinids	*S. seminulina*	*G. altispira*	Age & Bioevent
1	3616	3625	3620.5	-	-	-	-	5:11	-	-	
2	3631	3634	3632.5	-	-	-	-	7:11	-	-	
3	3640	3643	3641.5	-	-	-	-	4:2	-	-	**6.13 Ma**: Sinistral neogloboquadrinids influx
4	3649	3652	3650.5	-	-	-	-	1:6	-	-	
5	3658	3661	3659.5	-	-	-	-	3:7	-	-	
6	3667	3670	3668.5	-	-	-	-	7:9	-	-	**6.36 Ma:** S/D change neogloboquadrinids
7	3676	3679	3677.5	-	-	-	-	5:2	-	-	
8	3685	3688	3686.5	-	-	-	-	3:1	-	-	**6.72 Ma:** top acme *G. scitula* dextral group (*G. nicolae*)
9	3694	3697	3695.5	3:0 c	-	-	0:10	3:0	-	-	
10	3703	3706	3704.5	31:2 c	-	-	0:7	7:3	-	-	
11	3712	3715	3713.5	19:0 c	-	-	0:4	1:0	-	-	
12	3721	3724	3722.5	7:0 c	-	-	0:4	3:1	-	-	
13	3730	3733	3731.5	27:2 c	-	-	11:2	2:0	-	-	
14	3739	3742	3740.5	3:0 c	-	-	-	-	-	-	**7.23Ma:** FCO *G. miotumida*
15	3748	3751	3749.5	-	-	-	9:2	-	-	-	
16	3757	3760	3758.5	-	-	-	5:4	4:0	-	-	
17	3766	3769	3767.5	-	-	2:0	3:7	2:0	2	-	
18	3775	3778	3776.5	Very high sand content; not suitable for biostratigraphy							
19	3784	3787	3785.5	-	-	1:0	6:8	3:0	-	1	
20	3793	3796	3794.5	-	-	-	0:1	-	-	-	
21	3802	3805	3803.5	Very high sand content; not suitable for biostratigraphy							
22	3814	3817	3815.5	Very high sand content; not suitable for biostratigraphy							
23	3826	3829	3827.5	-	-	2:0 c	8:4	1:0	26	4	**7.72 Ma**: LCO *G. menardii-4*; *S. seminulina*
24	3838	3841	3839.5	Very high sand content; not suitable for biostratigraphy							
25	3847	3850	3848.5	-	-	7:1 m	0:7	1:0	-	-	

26	3856	3859	3857.5	-	-	7:2 m	3:6	4:1	1	1
27	3865	3868	3866.5	-	-	14:2 m	7:0	-	-	-
28	3874	3877	3875.5	-	-	5:1 m	0:1	1:0	1	-
29	3883	3886	3884.5	-	-	4:0 m	2:0	1:1	-	-
30	3892	3895	3893.5	-	-	8:0 m	5:0	5:0	-	-
31	3901	3904	3902.5	-	-	-	1:0	9:0	-	-
32	3910	3913	3911.5	-	-	3:1 m	2:0	2:0	-	-
33	3919	3922	3920.5	-	-	3:0 m	2:1	3:1	-	-
34	3928	3931	3929.5	-	-	-	5:7	-	-	-
35	3937	3940	3938.5	-	-	-	-	-	-	-